Characterization of Triple-Negative Breast Cancer Preclinical Models Provides Functional Evidence of Metastatic Progression

Juan J. Arroyo-Crespo,[1] Ana Armiñán,[1*] David Charbonnier,[1,2] Coralie Deladriere[1#], Martina Palomino-Schätzlein,[4] Rubén Lamas-Domingo,[4] Jerónimo Forteza,[3] Antonio Pineda-Lucena,[4,5] María J. Vicent[1,2*]

[1]Polymer Therapeutics Laboratory, Centro de Investigación Príncipe Felipe, Av. Eduardo Primo Yúfera 3, Valencia 46012, Spain

[2]Screening Platform, Centro de Investigación Príncipe Felipe, Av. Eduardo Primo Yúfera 3, Valencia 46012, Spain

[3]Unidad Mixta Centro de Investigación Príncipe Felipe-Instituto Valenciano de Patología, Centro de Investigación Príncipe Felipe, Av. Eduardo Primo Yúfera 3, Valencia 46012, Spain

[4]Joint Research Unit in Clinical Metabolomics, Centro de Investigación Príncipe Felipe, Av. Eduardo Primo Yúfera 3, Valencia 46012, Spain

[5]Drug Discovery Unit, Instituto de Investigación Sanitaria La Fe, Avda. Fernando Abril Martorell, 106, 46026-Valencia, Spain

[*]Address Correspondence to: aarminan@cipf.es or mjvicent@cipf.es

[#] Current Address: PCAS Canada, 725 Trotter Street, St Jean sur Richelieu, QC J3B 8J8, Canada

RUNNING TITLE - Detailed preclinical characterization of triple negative breast cancer models

Novelty &Impact

For the first time, an in depth comparative analysis of two preclinical spontaneously metastatic TNBC orthotopic models (MDA-MB-231-Luc and 4T1) is described. We

This article has been accepted for publication and undergone full peer review but has not been through the copyediting, typesetting, pagination and proofreading process which may lead to differences between this version and the Version of Record. Please cite this article as doi: 10.1002/ijc.32270

discovered a metastatic switch in both models with immune system activation and serum-protein profile reconfiguration, which may support resistance to treatment and recurrence in TNBC. Importantly, we identified critical functional biomarkers and metabolomic signatures for metastasis progression that will facilitate the development of anti-cancer therapeutics.

KEYWORDS

Triple negative breast cancer, Nanomedicine, Preclinical models, Spontaneous metastasis, Metabolomics

Abstract

Triple-negative breast cancer (TNBC), an aggressive, metastatic, and recurrent breast cancer (BC) subtype, currently suffers from a lack of adequately described spontaneously metastatic preclinical models that faithfully reproduce the clinical scenario. We describe two preclinical spontaneously metastatic TNBC orthotopic murine models for the development of advanced therapeutics: an immunodeficient human MDA-MB-231-Luc model and an immunocompetent mouse 4T1 model. Furthermore, we provide a broad range of multifactorial analysis for both models that could provide relevant information for the development of new therapies and diagnostic tools. Our comparisons uncovered differential growth rates, stromal arrangements, and metabolic profiles in primary tumors, and the presence of cancer-associated adipocyte infiltration in the MDA-MB-231-Luc model. Histopathological studies highlighted the more rapid metastatic spread to the lungs in the 4T1 model following a lymphatic route, while we observed both homogeneous (MDA-MB-231-Luc) and heterogeneous (4T1) metastatic spread to axillary lymph nodes. We encountered unique metabolomic signatures in each model, including crucial amino acids and cell membrane components. Hematological analysis demonstrated severe leukemoid and lymphoid reactions in the 4T1 model with the partial reestablishment of immune responses in the immunocompromised MDA-MB-231-Luc model. Additionally, we discovered β-

immunoglobulinemia and increased basal levels of G-CSF correlating with a metastatic switch, with G-CSF also promoting extramedullary hematopoiesis (both models) and causing hepatosplenomegaly (4T1 model). Overall, we believe that the characterization of these preclinical models will foster the development of advanced therapeutic strategies for TNBC treatment, especially for the treatment of patients presenting both, primary tumors and metastatic spread.

Introduction

Triple negative breast cancer (TNBC, lacking progesterone receptor (PR), estrogen receptors (ER), and human epidermal growth factor receptor 2 (HER2) expression) represents ~15-20% of newly diagnosed cases[1] and a complex molecular landscape, low detection rate, and aggressive/highly-proliferative nature result in poor prognosis and heterogeneous behavior in patients. Rapid growth rates and prominent lymphoplasmacytic inflammatory infiltrates due to host immune responses promote metastasis to the lungs, liver, and brain metastasis and the frequent lymphatic system involvement that impedes focal treatment, favors recurrence, aggravates the clinical situation, and lowers survival rates[1]. Rapid tumor evolution also leads to the development of an inner hypoxic and a subsequent necrotic core[2], promoting multiple drug resistance (MDR) and poorer prognosis[3].

TNBC currently lacks targeted therapeutics[1], and current treatment strategies provide heterogeneous responses/outcomes[2]. Additionally, no standardized treatment for metastatic TNBC exists, therefore representing a critical unmet clinical need[3]. Multistage animal models represent crucial translational research platforms for the testing and validation of experimental therapies; however, the lack of accurately characterized models that faithfully

mimic the pathological features of human TNBC, including spontaneous metastasis or multiple side alterations, frequently hampers research[4]. Currently employed metastatic mouse models mimic advanced stage disease, but the requirement for infusions of high concentrations of aggressive breast cancer (BC) cells[4], the need to resect the primary tumor to allow metastasis, or slow metastatic development limits the application of these models.

We now present the differential features of two preclinically relevant spontaneously metastatic TNBC mouse models. First, the well-established 4T1 model[5] developed in an immunocompetent (BALB/c) background (representing the murine disease) and second, the MDA-MB-231-Luc model[6] established in immunodeficient (NOD/SCID) background (representing the human disease, and more specifically, the mesenchymal stem-like subtype).

Within this study, we carried out a broad and detailed characterization of disease progression in each model and assessed for functional biomarkers, key metabolites, and differential cytokines considered crucial for prognosis. Furthermore, we analyzed the suitability for the application of preclinical models in the development/translation of advanced therapeutics for TNBC treatment, as features such as the enhanced permeability and retention (EPR) effect have also been explored[6].

Materials and Methods

Cell Culture Conditions

The 4T1 cell line and MDA-MB-231-Luc cell line were maintained in RPMI1640 media + 10% heat-inactivated fetal bovine serum (FBS) and DMEM/F12 media (Gibco) + 10% FBS + 500 μg/mL geneticin (Gibco), respectively, under standard tissue culture conditions. In both cases, media was replaced every 2 - 3 days and cells passaged once cultures reached 80% confluence. Transfection stability and lack of HER-2, PR, and ER expression in MDA-MB-

231-Luc cells were confirmed before inoculation (Also, see supplementary information (**SI**) **Fig. S1**).

Mouse Strains

Eight-week-old female inbred immunocompetent BALB/c (BALB/cOlaHsd) mice and the immunodeficient non-obese diabetic NOD/SCID (NOD.CB17-*Prkdc*^{scid}/NCrHsd) mice used herein were purchased from Envigo Laboratories Inc. (Spain, EU). 4 to 8 animals have been used for each experimental time point.

Study of the Enhanced Permeability and Retention Effect as a Functional Biomarker

To study vascular permeability, we followed previously described protocols[7]. See **SI** for detailed information.

Establishment of Spontaneously Metastatic Primary Tumor Models

4T1 orthotopic tumors were induced via subdermal inoculation of 5 x 10^5 4T1 early passage cells suspended in 100 µl of Matrigel (20%) in the second left mammary fat pad of BALB/c females under inhalatory anesthesia (3% sevoflurane in 100% oxygen). Following the same experimental conditions, MDA-MB-231-Luc tumors were established using 3 x 10^6 early passage cells in NOD/SCID mice. Tumors were morphometrically evaluated daily with an electronic caliper and tumor volumes obtained considering a spheroidal tumor shape. Metastases in organs of interest in the 4T1 model were isolated and evaluated following a previously described protocol[5].

Non-Invasive Imaging Techniques to Monitor Metastasis

Bioluminescence (BLI) by IVIS®

MDA-MB-231-Luc cells were tracked using IVIS® technology. For BLI analysis, mice were anesthetized and received a subdermal injection of 150 mg/kg D-luciferin (Gold BioTechnology, USA). Images were acquired using automatic camera settings and BLI data quantified with Living Image software (PerkinElmer, Japan) in terms of photons per second. For detailed protocols, see **SI**.

Positron Emission Tomography-Computed Tomography (PET-CT) Analysis

For PET-CT analysis, animals were kept without food for 14 h before radiotracer administration for PET and housed at a constant temperature of 21ºC. The average mouse weight was 19.2±0.7g, while the average blood glucose level was 47.2±10.1 $mg.dl^{-1}$. Anesthesia was induced by inhalation of isoflurane (4% in 100% oxygen) and maintained at (1.5% in 100% oxygen). See **SI** for further details.

Blood Collection and Analysis

At defined time points, mice were sacrificed under a CO_2 atmosphere. Blood was immediately extracted by cardiac puncture. Serum was isolated and analyzed using an automated hematologic analyzer (Sysmex XT-2000i). Serum protein content was measured using an automated capillary electrophoresis system (Capillarys 2, Sebia, France). See **SI** for additional details.

Histopathological Analysis and Imaging

Histopathological analysis employed conventional tissue preparation and paraffin inclusion (see SI). Tissue slides of interest were scanned with a Panoramic 250 Flash III slide scanner and processed with CaseViewer software (3DHISTECH Ltd, Budapest, Hungary). We provide a detailed list of the antibodies employed in the **SI** section (**Fig. S11**).

Metabolomics Profiling by NMR

Metabolomic sampling and processing were carried out according to previously described protocol[8]. See **SI** for further details.

Exosome Isolation, Measurement, and Quantification from Mouse Blood Serum

Serum exosome isolation was performed by serial differential centrifugations of fresh serum isolated from blood through centrifugation (see **SI** for details of the process). For exosome measurement and quantification, purified exosomes were diluted with PBS buffer (100 – 5000 times) to reach a particle concentration in the operational range for nanoparticle

tracking analysis (NTA) ($2 \times 10^8 - 2 \times 10^9$ particles/ml). Exosomes were then quantified and measured using the Nanosight NS300 (Malvern Instruments, UK).

Results

Comparison of TNBC Model Primary Tumor Development

Primary morphological analysis demonstrated that 4T1 tumors grew exponentially and homogeneously, reaching a cylindrical form after day (D)24 (**Fig. S2**). Subsequent analysis demonstrated slower initial growth kinetics for MDA-MB-231-Luc tumors compared to 4T1 up to ~D30, finally acquiring an amorphous cylindrical shape at D42 (**Fig. S2**). Primary tumors in both models exhibited the typical stromal progression of most solid tumors, including inner necrotic region development[9], although with marked differences in growth kinetics and stromal arrangement (**Fig. S3A, B).**

Analysis of tumors at the experimental endpoints demonstrated that the internal necrotic tissue presented cellular debris with diffuse margins, pyknotic nuclei, and karyorrhexis in both models (See H&E sections in **Fig. 1A, B**). While H&E tumor sections in 4T1 tumors identified a spheroidal concentric necrotic core surrounded by homogeneous concentric transition rings followed by a concentric proliferative region, MDA-MB-231-Luc tumors presented a more gelatinous necrotic core with heterogeneous spread of necrosis throughout the tumor stroma (**Fig. 1A, B)**. Overall, the stroma surrounding MDA-MB-231-Luc tumors presented lower cellular density and tumors evolved as soft and flexible solid masses (**Fig. S3A, B).** Both animal models developed fungating lesions (round, non-bleeding skin ulcerations with firm inflamed borders above the mammary gland) that appeared during the first week of 4T1- and the second week of MDA-MB-231-Luc-tumor development, in line with human wound development subtypes[10] (**Fig. S2**).

Cytokeratin (CK)-AE1/AE3 immunostaining confirmed the epithelial nature of tumor cells, with expression varying between both region, and model. Factor VIII immunostaining demonstrated similar tumor neovasculature and undamaged endogenous blood vessels in both models, indicating a slightly vascularized tumor stroma **(Fig. 1A, B)**. We subsequently

evaluated region-dependent proliferative rates by Ki-67 immunostaining and confirmed increased cell growth rates in outer regions of both tumors. We summarize data on immunohistochemical tumor markers in **Fig. S3A.**

We also morphometrically evaluated volume during tumor development in both models, discovering marked differences in growth kinetic profiles (**Fig. 1C**). We observed a ~2-fold greater tumor growth rate for the 4T1 model (reaching ~1.0 cm^3 at D24) when compared to the MDA-MB-231-Luc model (reaching ~1.0 cm^3 at D42), despite notable differences in the number of inoculated cells (5 x 10^5 vs. 3 x 10^6, respectively).

Subsequent quantification of maximum tumor permeability (related to the EPR effect[7]) established three-fold greater permeability for the MDA-MB-231-Luc model when compared to the 4T1 model (33% injected dose (ID)/gram of tumor (g) at ~D14 vs. 13% ID/g at D10, respectively, when analyzing tumors at ~0.1 cm^3) (**Fig. 1D)**.

Tumor density analyses reflected differential stromal arrangements, as previously noted (**Fig. 1E**). 4T1 tumors initially displayed high density at early development time points (~3 g/cm^3), which then decreased progressively over two weeks to ~1.5 g/cm^3. In contrast, MDA-MB-231-Luc tumors displayed a more homogeneous density during tumor development, rising from 1.0 g/cm^3 to 1.4 g/cm^3 over the experimental time frame.

Additional metabolomics analysis supported differences in tumor growth kinetics observed between models; 4T1 tumors displayed increased levels of guanosine and uracil (metabolites related to cell growth and proliferation, **Fig. 1F, G**) and cholesterol and phospholipids (critical cell membrane components, **Fig. 1H, I**), when compared to the MDA-MB-231-Luc tumors.

Importantly, the tumor histopathological study at model endpoints also demonstrated a relationship between MDA-MB-231-Luc tumors, but not 4T1 tumors, and lipid burden (**Fig. 1A, B)**. We observed disperse accumulation of adipocyte lobes from early stages of MDA-MB-231-Luc tumor development, with adipocytes distributed throughout the proliferative tumor region **(Fig. S3B, C).** According to their reduced size and distribution pattern within the tumor stroma and further Interleukin (IL)-6 and IL-1β immunostaining[11, 12] (**Fig. 1J)**, we

consider these adipocytes as cancer-associated adipocytes (CAA). Interestingly, metabolomic comparisons revealed significantly increased triacylglycerol (TAG) levels for MDA-MB-231-Luc tumors, a lipid whose synthesis/hydrolysis is controlled by adipocytes, agreeing with histopathological findings (**Fig. 1H, I**).

Comparison of TNBC Model Spontaneous Metastatic Landscape

4T1 tumors metastasize to liver, lungs, bones, and brain at advanced stages, and we employed intrinsic resistance to 6-thioguanine (6-TG) to quantify metastatic cells[13]**.** MDA-MB-231-Luc tumors produce multiple organ metastasis after intravenous cancer cell inoculation or after tumor resection[14]; however, to the best of our knowledge, no study has reported spontaneous metastatic spread from unresected MDA-MB-231 tumors in NOD/SCID mice (e.g., see Ref. [15]). In both models, we observed a very low incidence of brain, bone, and liver metastases, but high levels of lung and axillary lymph node (ALN) metastasis (**Fig. 2**), a finding that correlates with the TNBC clinical scenario. Therefore, our studies focused on these two major metastatic sites**.**

Lungs from the 4T1 model revealed evident sub-pleural metastases from D8, although we discovered the first evidence of discrete micro-metastasis from D3 (**Fig. S4**). Between D8 to D16, lungs presented with perivascular metastatic nodules following a predominantly sub-pleural pattern[16]. H&E staining identified prominent metastatic progression leading to disperse necrotic regions from D14 (**Fig. 2A**). Additionally, macroscopic examination identified increased tissue hyperemia concomitant with metastasis progression; however, we did not observe this trend in MDA-MB-231-Luc lungs (**Fig. 2B).**

Metastatic burden in MDA-MB-231-Luc appeared later than in the 4T1 and exhibited higher variability. Macroscopic lung evaluation uncovered first signs of lung metastases at ~D28 as homogeneously disperse nodes, with intraalveolar and intrabronchiolar metastatic infiltrations present throughout the lung parenchyma (**Fig. 2A, B**). Subsequently, lungs became slightly hyperemic and displayed signs of damage (**Fig. 2B**). We confirmed metastasis and enhanced proliferation in both models using CK-AE1/AE3 and Ki-67 immunostaining, respectively (**Fig. 2A, B**, and **Fig. S3A, C**). Overall, we observed higher

lung metastasis and lesser implication of the subpleural region in the MDA-MB-231-Luc compared to the 4T1 model.

Comparisons of healthy and metastatic lungs at the metabolomics levels established significant alterations in both models. Analysis of corresponding Orthogonal Projections to Latent Structures Discriminant Analysis (OPLS-DA) models revealed similar metabolic changes for the 4T1 and MDA-MB-231-Luc models (e.g., taurine, glutamate, UDP-N-acetylglucosamine), while other metabolites experienced variations of opposite sign (e.g., lysine, tyrosine). Furthermore, comparisons between metastatic and healthy lungs also uncovered several unique metabolic changes (e.g., 4T1: phenylalanine, arginine, aspartate; MDA-MB-231-Luc: glutathione, glycerophosphocholine) (**Fig. 2C-F**).

At the macroscopic level, inguinal lymph node (ILN) metastases appeared in most 4T1 animals, and those with ILN metastases suffered from rapid ALN spread. Direct ALN metastasis without ILN involvement rarely occurred (**Fig. 2C**). However, we seldom found metastases on the right side of the body (side of inoculation) and so we focused on metastatic development from tumor to left ALN following the afferent lymphatic vessel. 4T1 ALNs appeared macroscopically normal until D17, after which we observed metastasis (**Fig. 2G)**. Histopathological studies revealed nodes with varying degrees of physiological activation and swelling in the absence of metastasis until D10, and the majority of mice displayed similar characteristics by the endpoint (Inset **Fig. 2G)**. However, some 4T1 tumor-bearing mice exhibited paracortical metastatic foci within the node hilus from D13. Mice with similar characteristics displayed widespread metastatic invasion of the ALN at D20 of tumor development. By D24, mice exhibited almost complete ALN invasion with normal morphology loss.

MDA-MB-231-Luc model macroscopic studies discovered lower variability in ALN invasion when compared to the 4T1 (**Fig. 2H)**. We observed no signs of metastatic spread in the first three weeks of MDA-MB-231-Luc tumor development; however, all ALNs presented with signs of medullary sinusoidal metastasis at D21-28 (inset **Fig. 2H)**. As expected, ALN swelling directly correlated to metastasis due to the lack of lymph node immunoreactivity and

immune-related swelling. We also discovered more prominent metastasis to the left ALN in the MDA-MB-231-Luc model at advanced tumor development stage (**Fig. 2H**). **Figure S3** and **S4** summarize findings related to primary tumor and spontaneous metastasis landscape and **Figure S5** depicts time-frame metastatic spread in MDA-MB-231 ALNs.

Non-invasive imaging of Primary Tumor and Metastasis Development in TNBC Models

^{18}F-fluorodeoxyglucose uptake by positron emission tomography (^{18}F-FDG-PET) and computed tomography (CT) permitted *in vivo* analysis of 4T1 tumor progression[17]. **Figure 3A** depicts a three-dimensional view of tumor development displaying uniform radiotracer uptake by the spheroidal tumor mass until D3. We observed the development of an inner tumor core from D10, growing concentrically within the tumor mass, confirming previous findings (**Fig. S3**) and coinciding with maximal EPR effect (**Fig. 1D**). Analysis displayed in **Figure 3A** confirmed tumor core necrosis via the lack of radiotracer uptake. At endpoint, the necrotic region constituted ~80% of total tumor volume, and PET analysis confirmed metastasis in the left ALN only (**Fig. 3B, Fig. S6**).

Inherent luciferase activity in MDA-MB-231-Luc cells permitted the *in vivo* tracking of tumor progression and quantification of distal metastasis by bioluminescence imaging (BLI) using the IVIS® system (**Fig. 3C**). Tumors grew uniformly until D28, after which they became amorphous, with a loss of bioluminescence, again evidencing the necrotic core. **Figure 3C** also confirmed the uniform appearance of left ALN metastasis at D28 as demonstrated by histopathology (**Fig. 2D**). BLI analysis at D35 revealed increased left ALN metastasis with extravasation to the right ALN, the advancement of tumor core necrosis, and metastatic spread to surrounding tissues (**Fig 3C**). At endpoint, all mice displayed increased metastatic growth to the left ALN, invasion of the right ALN, and metastatic growth development in abdominal and thoracic regions (**Fig. S6)**.

Dynamic PET/CT analyses demonstrated a hypodense region within MDA-MB-231-Luc tumors at endpoint (**Fig. 3D** - red arrow); however, we observed a thinner ^{18}F-FDG labeled ring in the peritumoral region indicative of lower glucose metabolism at the tumor site. Additionally, we observed evidence of radiotracer uptake in abdominal lymph nodes around

the tumor site (**Fig. 3D** inset). **Fig. 3E** shows significantly swollen left ALNs by CT. By PET, we detected the expected metastatic growth with the highest uptake located close to the afferent region of the left ALN and metastatic spread to the right ALN in the absence of swelling (as shown by CT) (**Fig. 3E** - yellow arrows). By CT, we also observed lung metastasis following the so-called miliary pattern[18], which describes innumerable small metastases of variable-size within the parenchyma (**Fig. S4C**; consistent with **Fig. 3E**).

Comparison of TNBC Model Hematological Parameters

The hematological study depicted the development of systemic pathologies during tumor growth, including a marked tumor-derived inflammatory response with anemia, thrombocytosis, reticulocytosis, leukocytosis, and subsequent lymphocytosis (**Fig. 4** and **Fig. S7**). This profile evolved during tumor development, although we observed model-specific alterations related to immune system status with significantly higher levels of leukocytes/lymphocytes at later stages in the 4T1 model (**Fig. 4)**. Both models exhibited reduced erythrocyte levels (~8-10%) during tumor development, correlating to imbalanced medullary/extra-medullary hematopoiesis (**Fig. 4A, B)**. We found more pronounced anemia in the 4T1 model with hemoglobin levels diminishing gradually (**Fig. S7)**. Although more pronounced in the 4T1 model, we also discovered a robust increase in reticulocytes in both models; however, in contrast, we found significantly higher thrombocyte levels in the MDA-MB-231-Luc model (~800 $g.L^{-1}$ vs. ~ 400 $g.L^{-1}$) at endpoints (**Fig. 4A, B)**.

While a severe leukemoid reaction occurred from D10 in the 4T1 model (~160 $g.L^{-1}$), we only observed a slight effect in the MDA-MB-231-Luc model (~27 $g.L^{-1}$) close to endpoint (**Fig 4A, B**). In both models, segmented neutrophils accounted for ~33% of leukocyte number before tumor cell inoculation and ~85% at the endpoints. We also observed a differential lymphoid reaction between the models, in agreement with leukocyte counts. Wright-stained blood smears confirmed results by allowing comparisons with data from healthy mice with tumor model endpoint data (**Fig. S7)**. Although we observed a more moderate response in MDA-MB-231-Luc, both models exhibited extensive granulocytosis (left shift) with predominant levels of polynuclear-segmented leukocytes.

Immunophoretic analysis of blood serum revealed a significant and sudden increase in gamma-globulin and alpha-2-globulin levels and a decrease in albumin levels at D42 in the MDA-MB-231-Luc model (**Fig. 4C**). Moreover, we found increased beta globulin bands in 4T1 (D3) and MDA-MB-231-Luc (D35) models, coinciding with the first evidence of lung metastasis (**Fig. 4C, D**).

Exosomes play crucial roles in conditioning the pre-metastatic niche[19], and we employed NTA of peripheral blood serum to assess exosomal dynamics during tumor progression. We discovered peak exosome levels on the first appearance of metastasis (D3) in 4T1 (**Fig. 4E, S8**), before returning to basal levels. However, we did not observe any fluctuations during tumor progression in the MDA-MB-231-Luc model.

Directly correlated with the immune system status, inflammatory response markers may predict clinical outcomes in cancer patients, and so, we evaluated the neutrophil-lymphocyte-ratio (NLR), finding a rapid increase from D6 in the 4T1 model (**Fig. 4F**). As an innate immune system effector, the complement system constitutes the first barrier against non-self-cells and plays a decisive role in tumor growth[20]. In agreement, 4T1 animals displayed increasing levels of C-3 protein from D20 (**Fig. 4G).**

Dysregulated Bone Marrow Hematopoiesis in TNBC Models: A role for G-CSF in Extramedullary Hematopoiesis

Initial macroscopic organ analysis indicated acute splenomegaly (0.6% to 4% total body weight from D6 to D24) and slight hepatomegaly (4.8% to 6% total body weight over 24 days) (**Fig. S9A, B**) in the 4T1 model[21], but not the MDA-MB-231-Luc model.

Histopathological studies of bone marrow uncovered reduced megakaryocytosis (Factor VIII), reduced myeloid cell precursors (myeloperoxidase), and enhanced granulocytosis (CD-15) compared to healthy tissues (**Fig. 5A)**, supporting extramedullary hematopoiesis (EH) promoted by bone marrow myelosuppression (in agreement with previous hematological findings). Analysis of the enlarged spleen of the 4T1 model supported EH by reactive megakaryocytic hyperplasia, as evidenced by large numbers of Factor VIII-positive megakaryocytes, and ongoing erythropoiesis, as evidenced by Glycophorin A-positive

erythroid-precursors and mature erythrocytes (**Fig. 5B**). Further studies revealed increased cellularity and congested red pulp with hyperplasia due to elevated reactive hematopoiesis (**Fig. S9C, D**). Studies of the MDA-MB-231-Luc model normal-sized spleen highlighted reactive megakaryocytic hyperplasia as the unique pathological consequence of EH (**Fig 5B**).

In the 4T1 model, we observed overt signs of EH in the liver, as evidenced by increased myeloid precursor cell[22-24] (MPC) perivascular infiltration into the surrounding hepatic arteries starting from D3 (**Fig. S9E**). At later stages, MPCs entered the liver parenchyma to induce reactive megakaryocytic hyperplasia (**Figure 5B**). In contrast, MDA-MB-231-Luc model liver developed no significant macroscopic or histopathological abnormalities (**Fig. 5B**).

To understand EH origin, we conducted immunoassays to analyze circulating granulocyte colony stimulating factor (G-CSF) levels[25]. We discovered increasing levels of total G-CSF in 4T1 model peripheral blood at early stages of tumor development (**Fig. 5C**), in agreement with previous studies in immunocompetent mouse models[26]. We also discovered increasing levels of tumor- and host-derived G-CSF during MDA-MB-231-Luc tumor progression **(Fig. 5C)**. Of note, only *in vitro* studies have previously shown G-CSF secretion from MDA-MB-231 cells[27]. High human G-CSF levels in MDA-MB-231-Luc started increasing from D28 (**Fig. 5D**) and correlated to the previously observed leukemoid/lymphoid reactions.

Discussion

The accelerated development of advanced anti-cancer therapies requires preclinical models and the identification of functional biomarkers to facilitate clinical translation[28] and identification of patients who could benefit from therapies[29]. In this study, we report the exhaustive characterization of relevant preclinical TNBC mouse models regarding systemic landscape, metastatic foci, and metabolic alterations, paying particular attention to functional biomarkers. Both models develop homogeneous primary tumors with subsequent ALN and lungs metastasis, faithfully mimicking critical features of the human disease. Therefore, these

models offer a useful platform for testing/validation of advanced anticancer therapeutics, especially for the treatment of patients presenting with both primary tumors and metastasis.

Modeling Capacities of the 4T1 and MDA-MB-231-Luc TNBC Models

The rapid tumorigenic development encountered for the 4T1 model offers a rapid and straightforward means to assess treatment outcomes in an immunocompetent model. Model characteristics include aggressive primary tumor evolution as densely packed masses with slight anemia, thrombocytosis, and reticulocytosis in the short term, and an acute leukemoid reaction with lymphocytosis and complement system activation in the mid-to-long term. In comparison, the MDA-MB-231-Luc model displayed slower tumor growth with marked spontaneous inclusion of CAAs, known to exhibit an activated phenotype linked to the acquisition of a pro-invasive effect of surrounding tumor cells[12]. Therefore, high CAA content of MDA-MB-231-Luc tumors may serve as a faithful model to study this phenomenon and develop treatments to avoid adipocytic pro-tumorigenic effects. Furthermore, high lipid content and low cellular density in the tumor stroma generated a softer tumor mass with a three-fold higher EPR effect, thereby providing a model to assess EPR-related passive tumor accumulation, especially important for the effectiveness of nanomedicinal approaches to cancer treatment[7, 30, 31]. The flexibility and permeability of the MDA-MB-231-Luc model stroma may also provide a means to assess intratumoral administration strategies[32].

The metabolomic comparison of 4T1 and MDA-MB-231-Luc primary tumors suggests that specific metabolic alterations could explain the differences observed in growth rates, with guanosine and uracil (a pyrimidine derivative) the two most relevant soluble metabolites contributing to model discrimination. Interestingly, Tayyari *et al.*[33] reported that TNBC tumors displayed increased pyrimidine synthesis and elevated levels of myoinositol and taurine, similar to findings in our 4T1 primary tumors. Metabolomic analysis of organic extracts provided further evidence for lipidic reprogramming in TNBC development and progression; in particular, 4T1 primary tumors displayed higher concentrations of cholesterol and phospholipids. These alterations reflect the avidity of proliferative cancer cells for lipids

and cholesterol[34], a characteristic now considered a hallmark of cancer aggressiveness[34, 35]. MDA-MB-231-Luc primary tumors also displayed high levels of TAGs, whose hydrolysis in adipocytes adjacent to cancer cells generates free fatty acids for use as an energy source by tumor cells for tumor progression[34] .

We observed spontaneous lung and ALN metastasis in both models; however, while studies suggest that the 4T1 model develops lung metastasis via the hematogenous route[13], we discovered earlier evidence of distal metastasis and subsequent rapid development predominantly through the lymphatic system, as observed in two recent studies[36, 37]. Therefore, the 4T1 mouse model is ideal for the development and validation of lymph-targeted anti-cancer therapies[38]. Additionally, alterations to the complement system in the 4T1 model may provide a prognostic marker of disease progression or even a sign of treatment efficiency when using non-immunogenic therapeutics (a safety requirement for systemic administration).

The Role of G-CSF as a Critical Functional Biomarker of Metastatic Progression

The colony-stimulating factor (CSF) subfamily of glycoproteins play crucial roles in inflammatory cell activation[39], bone marrow cell mobilization into the peripheral blood, and immune system activation[40]. Increasing levels of G-CSF during 4T1 tumor progression[26] may trigger passive compensatory EH and the concomitant leukemoid reaction with prominent hepatosplenomegaly[26]. The leukemoid reaction is a well-described paraneoplastic affection, arising in ~15% of cancer patients, proposed as a prognostic marker for BC[41] thereby ratifying the suitability of our 4T1 model as preclinical BC model.

The MDA-MB-231-Luc model presented similar hematological parameters to the 4T1 model at early stages; however, we did not observe a leukemoid reaction accompanying tumor growth, and the first evidence of metastasis occurred at later time points through the hematological pathway. Importantly we observed that tumor- and host-derived G-CSF release concomitant with metastasis, led to the partial restoration of the immune system (granulocytosis and lymphocytosis) suggesting a “metastatic switch” appearing from the fourth week to trigger an immunological response in the immunosuppressed NOD/SCID

mouse model. This suggests that stromal cells and/or host tumor-infiltrating cells also represent a significant G-CSF source[42]. Although the reduced immunological competency of the host does not permit extended adaptive splenomegaly or hepatomegaly in this model, we observed slight passive EH in the spleen as a response to bone marrow myelosuppression. Surprisingly, we only observed lung metastasis from D28, concomitant with human G-CSF release. Studies have proposed the indirect role of G-CSF in pre-metastatic niche formation[43], a finding supported by our MDA-MB-231-Luc model discoveries. Therefore, we propose circulating G-CSF levels as a prognostic indicator of disease and more importantly, the inhibition of cytokines such as CSFs as a promising therapeutic approach alone or in combination with metastatic inhibitors. We do note that the possible role of either human or host G-CSF in the immune system reactivation of the NOD/SCID mice remains unresolved; although the leukemoid reaction triggered by the release of G-CSF may be responsible for metastasis spread.

Our work emphasizes the active role of the immune system in metastatic spread in both models[44]. We suggest, after the sudden changes at week four, that a quiescent MDA-MB-231-Luc tumor subpopulation reactivates through a likely "metastatic switch". Several tumor-derived factors could be involved in the generation of pre-metastatic niche, and their overexpression could be a prerequisite for metastasis development.

Other Biomarkers and Predictive Factors

Exosomes have emerged as regulators of inter- and intra-cellular communication and can "tailor" the pre-metastatic niche for engraftment of cancer cells[19]. Interestingly, the 4T1 model displayed significantly increased circulating blood exosomes at D3, simultaneous with the first evidence of lung metastasis, suggesting its active role in lung metastasis establishment[19]. However, we did not find any modulation in exosome levels in MDA-MB-231-Luc.

The prompt hyper-β-immunoglobulinemia detected in both models coincided with first signs of lung metastasis. Transferrin overexpression may be connected to neovascularization to influence metastatic capacity in BC[45]. Transferrin-like lipoproteins can specifically stimulate

metastatic cell growth[46]. Similarly, β-lipoprotein (LDL) is intimately involved in angiogenic regulation, with a direct connection between LDL levels and metastatic progress[47]. In this context, our metabolomics analyses confirmed that lipid metabolism alterations closely associates with TNBC malignancy and metastatic progression to the lungs.

Finally, studies have demonstrated that NLR associates with poorer prognosis in human cancers[48]; high NLR associates with reduced disease-free survival (DFS). Applying this prognostic factor in our 4T1 model, NLR values indicate worse prognosis from D6-10, mimicking advanced stages of the disease and providing a tool to develop therapeutics devoted to recurrent or metastatic scenarios.

Metabolomic Metastatic Signature

Metabolomic analysis of lung tissues revealed distinct signatures for both models. Some metabolites exhibited the same trend when comparing metastatic and healthy lung tissues (taurine, glutamate, UDP-NAG, glucose), reflecting common alterations. For example, the metabolism of glutamate/glutamine and taurine/hypotaurine plays a significant role in TNBC[33] and UDP-derivatives have been linked to metastasis[49]. A second important group of metabolites, mostly composed of amino acids, exhibited changes in the opposite direction when comparing metastatic and healthy lung tissues. The differences in amino acids levels may relate to different growth kinetics; much faster for the 4T1 model therefore requiring more energy. Of note, several amino acids that exhibited lower concentrations in the MDA-MB-231-Luc model metastatic lung (i.e., leucine, isoleucine, and valine) are branched amino acids (BCAA) and studies have indicated an association between increased concentrations of BCAA and chemotherapy-induced apoptotic processes[8]. Interestingly, the ratio of choline/GPC indicates the acidic nature of metastatic tumors, since lower pH (typical of tumor cells) leads to decreased PC and increased GPC[50]. High glutamine consumption correlates with the essential function of glutaminase in TNBC development[51]. Decreased creatine phosphate levels, perhaps related to hypoxic regions within the metastasis[52], also correlate with the reduced pH characteristic of tumors.

We also found several unique metabolic changes for each model. In 4T1 metastatic lungs, we discovered increased phenylalanine levels[53] (related with advanced stages of the disease), aspartate[8] (upregulated glutaminolysis) and ATP+ADP (fueling metastatic survival). Analysis of MDA-MB-231-Luc metastatic lungs revealed a specific increase in glutathione levels, a molecule that plays protective and pathogenic roles and promotes chemoresistance[54], and GPC levels. Overall, the metabolomic signature for lung metastases in each model reflects the different molecular and biochemical mechanisms associated with metastatic spread, which could be employed as a biomarker for disease monitoring during preclinical evaluation (see also **Fig. S10**).

One limitation of this study lies in the characterization of only one subtype, representing ~15% of all TNBC types. Therefore, a similar analysis of other TNBC subtypes would provide additional information that could be relevant from a clinical standpoint. We are also aware of the lack of tumor resection during the characterization of the metastatic spread to lungs, an intervention that would also closely mimic the clinical situation. Nevertheless, we believe that studying metastasis in the presence of the primary tumor could aid the development of therapies for patients exhibiting both tumor modalities, who currently lack adequate preclinical models.

Conclusion

Within this present study, we describe the progression of two preclinical spontaneously metastatic TNBC models relevant for the development of anti-cancer therapeutics (summary of main features in Figure 6). We concentrated on the pathological features that ultimately drive anti-cancer treatment and, therefore, patient outcomes. Our exhaustive characterization demonstrated MDA-MB-231-Luc metastatic progression in the NOD/SCID model. We also discovered a metastatic switch in both models (MDA-MB-231-Luc and 4T1) with immune system activation and serum-protein profile reconfiguration, which may support resistance to treatment and recurrence in TNBC. The detailed characterization of relevant models such as these will help to foster the rational design of anti-cancer therapeutics. Importantly, we identified critical functional biomarkers including the EPR effect, G-CSF, CAA infiltration,

NLR, complement activation, and metabolomic signatures for metastasis progression that may further facilitate the development of anti-cancer therapeutics.

Authors' Contributions

Conception and design: J.J.A-C., A.A., M.J.V.

Development of experimental methodology: J.J.A-C., A.A., D.C., M.P-S., C.D.

Acquisition and interpretation of histopathological data: J.F., J.J.A-C., A.A.

Acquisition and interpretation of non-invasive imaging data: J.J.A-C., A.A., D.C.

Acquisition and interpretation of metabolomic data: A.P-L., M.P-S., J.J.A-C., A.A., R.L-D.

Analysis and interpretation of data: J.J.A-C., A.A., M.J.V., J.F., A.P-L., R.L-D.

Writing, review, and/or revision of the manuscript: J.J.A-C., A.A., M.J.V., J.F., A.P-L.

Study supervision: A.A., M.J.V.

Acknowledgments

The authors would like to thank Dr. Stuart P. Atkinson for his collaboration in manuscript preparation and English revision, Alejandro Robert from ACV Lab, for his advice in hematological evaluation of the models and interpretation, Emilio Giménez, César Molinos (Bruker) and Luisa Juan (Oncovision) for the PET/CT acquisition management and advice, and Irene Borredá for essential immunohistological support. This work has been supported by the European Research Council (grant ERC-CoG-2014-648831 “MyNano”) and the Spanish Ministry of Science and Innovation (SAF2013-44848-R, SAF2014-53977-R, SAF2016-80427-R, SAF2017-89229-R). Part of the equipment employed in this work has been funded by Generalitat Valenciana and co-financed with FEDER funds (PO FEDER of Comunitat Valenciana 2014-2020).

FIGURE LEGENDS

Figure 1. Primary tumor development and immunohistological analysis of features. A) and **B)** Axial tumor H-E staining, demonstrating stromal arrangement and immunohistochemical study (CK-AE1-AE3, Factor VIII, and Ki-67) of tumor regions. Original magnification displayed in each image. **C)** Morphometric tumor analysis demonstrating differential grow kinetics of primary tumors in both models. **D)** EPR effect quantification of primary tumors. EPR_{MAX} was around 0.1 cm^3 for both tumor models, corresponding to D8 and D14 for 4T1 and MDA-MB-231-Luc, respectively. **E)** Tumor density determined by simple arithmetic calculation demonstrating a lighter stroma as result of lower cellular density and higher lipid content in the MDA-MB-231-Luc model. **F)** Multivariate modeling resulting from the analysis of primary tumors (**F** and **H**) OPLS-DA score plot representing the comparison between MDA-MB-231-Luc *vs.* 4T1 primary tumors (aqueous phase) (R^2 = 0.976 / Q^2 = 0.925) and organic phase (R^2 = 0.982 / Q^2 = 0.936), respectively. **G** and **I)** Metabolic changes for MDA-MB-231-Luc *vs.* 4T1 primary tumor (aqueous phase) and MDA-MB-231-Luc *vs.* 4T1 primary tumors (organic phase) comparisons. Statistical significance determined via ANOVA t-test, (*** $p<0.001$, ** $p<0.01$, *$p<0.05$). **J)** Representative images of CAAs with H&E staining and immunostaining with IL-1β and IL-6. CAAs from MDA-MB-231-Luc tumors exhibited extensive phenotypic changes. Subpopulations of adipocytes that infiltrated within tumor stroma expressed IL-1β and also IL-6 (but to a lesser extent)(CAAs indicated with red arrow heads). Note the diminished averaged sizes, a known characteristic feature of CAA.

Figure 2. Spontaneous lung and ALN metastatic development and immunohistological analysis. A) Representative images of 4T1 model lungs over time after necropsy and staining with H&E and immunostaining with CK-AE1/AE3 and Ki-67. 4T1 model lungs presented with prominent subpleural metastasis from D8 after tumor cell inoculation. Further analysis confirmed predominant pleural invasion, although intraparenchymal regions also appeared metastasized. Metastatic regions within the lungs as evidenced by CK-AE1/AE3 immunostaining and highly proliferative nature evidenced by Ki-67 immunostaining. **B)**

Representative images of MDA-MB-231 model lungs over time after necropsy and staining with H&E and immunostaining with CK-AE1/AE3 and Ki-67. The MDA-MB-231-Luc model developed metastasis later (D28) and the metastatic nodules appears disseminated throughout the lung parenchyma with predominant bronchioloalveolar pattern. Multivariate modeling resulting from the analysis of lung metastases. (**C** and **D)** OPLS-DA score plot representing comparisons between healthy lung tissue *vs.* metastatic lung (4T1) (aqueous phase; R^2 = 0.913 / Q^2 = 0.890) and healthy lung tissue *vs.* metastatic lung (MDA-MB-231-Luc) (aqueous phase; R^2 = 0.921 / Q^2 = 0.806), respectively. **E)** and **F)** Metabolic changes for healthy lung tissue *vs.* metastatic lung (4T1) (aqueous phase) and healthy lung tissue *vs.* metastatic lung (MDA-MB-231-Luc) (aqueous phase) comparisons, respectively. Statistical significance determined via ANOVA t-test, (*** $p<0.001$, ** $p<0.01$, *$p<0.05$). **G)** Evolution of ALN metastasis with time by H&E staining and CK-AE1/AE3 and Ki-67 immunostaining. The 4T1 model displayed heterogeneous metastatic invasion in ALN. The vast majority of animals presented metastasis in the left ALN at the experimental endpoint **H)** The MDA-MB-231-Luc model exhibited homogeneous ALN metastasis distribution. Left and right ALN are shown.

Figure 3. Non-invasive imaging techniques for in vivo visualization of primary tumor and metastatic landscape. A) PET/CT combination permitted in vivo monitoring of 4T1 primary tumor progression. Image reconstruction of overlapped CT and PET image acquisitions. Regions with different radiotracer uptake levels have been colored to facilitate interpretation: green: bladder identification (max ^{18}FDG caption); blue: tumor region identified by CT with high ^{18}FDG uptake. Red: tumor region identified by CT with low ^{18}FDG uptake rate. Note the increasing hypodense region developing in the tumor core corresponding to the necrotic core. **B)** ILN invasion observed close to the experimental endpoint, as seen in the axial projection of a representative 4T1 mouse. However, lung metastasis was not observed under our experimental conditions. **C)** Tumor growth and metastatic landscape demonstrated by BLI in the MDA-MB-231-Luc tumor model. ALN metastasis noted from D28, and tumor necrotic core noted from D35. **D)** Three-dimensional

projections of an MDA-MB-231-Luc representative mouse at the experimental endpoint. CT allowed for the delimitation of the tumor region (green region). Further PET analysis permitted the visualization of the peritumoral region, displaying a dark hollow indicative of tumor necrosis (inset, red arrow). Moreover, ILN metastasis was detectable with higher prominence on the left side (yellow arrows). **E)** Thoracic region in detail. Characteristic intraparenchymatous lung metastasis detected by CT (green arrows). In addition, the swollen left ALN detected by CT (red region), but only an active metastatic region was detected by PET (yellow region) within the ALN mass.

Figure 4. Hematological changes during tumor progression. Complete hemogram of 4T1 model (**A**) and MDA-MB-231-Luc (**B**). Proteinograms of peripheral blood in both models during tumor progression displayed in **C)** and **D)**. Beta hyperglobulinemia found in both models at the same time that lung metastasis evolved (D3 for the 4T1 model and D35 for the MDA-MB-231-Luc model). Data represent mean ± SEM. Statistical significance was determined via ANOVA t-test, (*** $p<0.001$, ** $p<0.01$, *$p<0.05$) The MDA-MB-231-Luc model displayed acute bands in the alpha immunoglobulin and gamma immunoglobulin, a profile compatible with ongoing inflammatory processes (increased alpha-2 globulin), while the unspecific hypoalbuminemia is consistent with any previously mentioned pathologies in a chronic scenario. **E)** Comparison of circulating exosome levels, quantified by NTA between both tumor models over time **F)** Neutrophil/Lymphocyte ratio (NLR). The MDA-MB-231-Luc mouse NLR is included for comparative purposes, although the immunocompromised character of the NOD/SCID mice does not permit a proper comparison. **G)** C3 complement system activation in the 4T1 tumor model.

Figure 5. Extramedullary hematopoiesis promoted by G-CSF occurred to a different extent between models and triggered mobilization of different myeloid precursors. In the first instance, G-CSF impedes the normal maturation of myeloid cell precursors in bone marrow (**A**). Representative images of bone marrow in healthy and experimental end points,

staining with H&E and immunostaining with Factor VIII, Myeloperoxidase, and CD-15. (**B**) 4T1 and MDA-MB-231-Luc cells secrete G-CSF, which blocks normal bone marrow hematopoiesis and activates extramedullary hematopoiesis by stimulating the release of immature myeloid precursors. The 4T1 model presented hepatosplenomegaly as result of erythropoiesis (Glycophorin A +) and megakaryopoiesis (Factor VIII +) in the spleen and also megakaryopoiesis in the liver. Additionally, multiple colonies of myeloid cell precursors were found in the liver. The MDA-MB-231-Luc model does not present with erythropoiesis-related hepatosplenomegaly (Glycophorin A –, in spleen and liver); however, prominent megakaryocytes were found in the spleen, as a result of strong megakaryopoiesis. (C) Levels of G-CSF in the 4T1 model over time. (D) Levels of human and murine G-CSF in the DA-MB-231-Luc model at progressive time points.

Figure 6. Summary of the main features of TNBC preclinical models. (**A**) Suggested suitability for different aspects of therapy development, demonstrating evident complementarity of the models for TNBC drug discovery and validation. (**B**) Timeline of TNBC tumor progression indicating main differential features between 4T1 and MDA-MB231-Luc regarding primary tumor, including stroma and metastatic sites (CAA: cancer-associated adipocytes, EPR: enhanced permeability and retention effect, G-CSF: granulocyte colony-stimulating factor, GPC: glycerylphosphorylcholine, TGA: triacylglycerol).

References

1. Bianchini G, Balko JM, Mayer IA, Sanders ME, Gianni L. Triple-negative breast cancer: challenges and opportunities of a heterogeneous disease. *Nat Rev Clin Oncol* 2016;**13**:674-90.
2. Tseng LM, Hsu NC, Chen SC, Lu YS, Lin CH, Chang DY, Li H, Lin YC, Chang HK, Chao TC, Ouyang F, Hou MF. Distant metastasis in triple-negative breast cancer. *Neoplasma* 2013;**60**:290-4.
3. Brouckaert O, Wildiers H, Floris G, Neven P. Update on triple-negative breast cancer: prognosis and management strategies. *Int J Womens Health* 2012;**4**:511-20.
4. Boichuk S, Galembikova A, Sitenkov A, Khusnutdinov R, Dunaev P, Valeeva E, Usolova N. Establishment and characterization of a triple negative basal-like breast cancer cell line with multi-drug resistance. *Oncol Lett* 2017;**14**:5039-45.
5. Pulaski BA, Ostrand-Rosenberg S. Mouse 4T1 Breast Tumor Model. *Curr Protoc Immunol* 2000;**39**:20.2.1-20.2.16.

6. Johnstone CN, Pattison AD, Gorringe KL, Harrison PF, Powell DR, Lock P, Baloyan D, Ernst M, Stewart AG, Beilharz TH, Anderson RL. Functional and genomic characterization of a xenograft model system for the study of metastasis in triple-negative breast cancer. *Dis Model Mech* 2018;**11**:dmm032250.
7. Maeda H, Tsukigawa K, Fang J. A retrospective 30 years after discovery of the enhanced permeability and retention effect of solid tumors: next-generation chemotherapeutics and photodynamic therapy-problems, solutions, and prospects. *Microcirculation* 2016;**23**:173-82.
8. Armiñán A, Palomino-Schätzlein M, Deladriere C, Arroyo-Crespo JJ, Vicente-Ruiz S, Vicent MJ, Pineda-Lucena A. Metabolomics facilitates the discrimination of the specific anti-cancer effects of free- and polymer-conjugated doxorubicin in breast cancer models. *Biomaterials* 2018;**162**:144-53.
9. Kobayashi H, Watanabe R, Choyke PL. Improving conventional enhanced permeability and retention (EPR) effects; What Is the appropriate target? *Theranostics* 2014;**4**:81-9.
10. Tilley C, Lipson J, Ramos M. Palliative wound care for malignant fungating wounds. *Nurs Clin North Am* 2016;**51**:513-31.
11. Lee J, Hong BS, Ryu HS, Lee H-B, Lee M, Park IA, Kim J, Han W, Noh D-Y, Moon H-G. Transition into inflammatory cancer-associated adipocytes in breast cancer microenvironment requires microRNA regulatory mechanism. *PLoS One* 2017;**12**:e0174126.
12. Dirat B, Bochet L, Dabek M, Daviaud D, Dauvillier S, Majed B, Wang YY, Meulle A, Salles B, Le Gonidec S, Garrido I, Escourrou G, et al. Cancer-associated adipocytes exhibit an activated phenotype and contribute to breast cancer invasion. *Cancer Res* 2011;**71**:2455-65.
13. H Heppner G, R Miller F, Malathy Shekhar PV. Nontransgenic models of breast cancer. *Breast Cancer Res* 2000;**2**:331.
14. Milsom CC, Lee CR, Hackl C, Man S, Kerbel RS. Differential post-surgical metastasis and survival in SCID, NOD-SCID and NOD-SCID-IL-2Rγnull mice with parental and subline variants of human breast cancer: Implications for host defense mechanisms regulating metastasis. *PLoS One* 2013;**8**:e71270.
15. Iorns E, Drews-Elger K, Ward TM, Dean S, Clarke J, Berry D, Ashry DE, Lippman M. A new mouse model for the study of human breast cancer metastasis. *PLoS One* 2012;**7**:e47995.
16. Donnem T, Hu J, Ferguson M, Adighibe O, Snell C, Harris AL, Gatter KC, Pezzella F. Vessel co-option in primary human tumors and metastases:an obstacle to effective anti-angiogenic treatment? *Cancer Med* 2013;**2**:427-36.
17. Marini C, Ravera S, Buschiazzo A, Bianchi G, Orengo AM, Bruno S, Bottoni G, Emionite L, Pastorino F, Monteverde E, Garaboldi L, Martella R, et al. Discovery of a novel glucose metabolism in cancer: The role of endoplasmic reticulum beyond glycolysis and pentose phosphate shunt. *Sci Rep* 2016;**6**:25092.
18. Schaller A, Beau-Faller M, Mennecier B, Renaud-Picard B, Weingertner N, Massard G, Quoix E. Lung adenocarcinoma with pulmonary miliary metastases and complex somatic heterozygous EGFR mutation. *Case Rep Oncol* 2014;**7**:769-73.
19. dos Anjos Pultz B, Andrés Cordero da Luz F, Socorro Faria S, Peixoto Ferreira de Souza L, Cristina Brígido Tavares P, Alonso Goulart V, Fontes W, Ricardo Goulart L, José Barbosa Silva

M. The multifaceted role of extracellular vesicles in metastasis: Priming the soil for seeding. *Int J Cancer* 2017;**140**:2397-407.

20. Pio R, Corrales L, Lambris JD. The role of complement in tumor growth. *Adv Exp Med Biol*. 2014;**772**:229-62.
21. Liu M, Jin X, He X, Pan L, Zhang X, Zhao Y. Macrophages support splenic erythropoiesis in 4T1 tumor-bearing mice. *PLoS One* 2015;**10**:e0121921.
22. Younos I, Dafferner A, Gulen D, C Britton H, Talmadge J. Tumor regulation of myeloid-derived suppressor cell proliferation and trafficking. *Int Immunopharmacol* 2012;**13**:245-56.
23. Younos I, Donkor M, Hoke T, Dafferner A, Samson H, Westphal S, Talmadge J. Tumor- and organ-dependent infiltration by myeloid-derived suppressor cells. *Int Immunopharmacol* 2011;**11**:816-26.
24. Cao Y, Slaney CY, Bidwell BN, Parker BS, Johnstone CN, Rautela J, Eckhardt BL, Anderson RL. BMP4 inhibits breast cancer metastasis by blocking myeloid-derived suppressor cell activity. *Cancer Res* 2014;**74**:5091-102.
25. Inra CN, Zhou BO, Acar M, Murphy MM, Richardson J, Zhao Z, Morrison SJ. A perisinusoidal niche for extramedullary haematopoiesis in the spleen. *Nature* 2015;**527**:466-71.
26. duPre SA, Hunter KW. Murine mammary carcinoma 4T1 induces a leukemoid reaction with splenomegaly: Association with tumor-derived growth factors. *Exp Mol Pathol* 2007;**82**:12-24.
27. Hollmén M, Karaman S, Schwager S, Lisibach A, Christiansen AJ, Maksimow M, Varga Z, Jalkanen S, Detmar M. G-CSF regulates macrophage phenotype and associates with poor overall survival in human triple-negative breast cancer. *OncoImmunology* 2015;**5**:e1115177.
28. Dhandapani M, Goldman A. Preclinical cancer models and biomarkers for drug development: new technologies and emerging tools. *J Mol Biomark Diagn* 2017;8:365.
29. Duncan R. Polymer therapeutics at a crossroads? Finding the path for improved translation in the twenty-first century. *J Drug Target* 2017;**25**:759-80.
30. Arroyo-Crespo JJ, Arminan A, Charbonnier D, Balzano-Nogueira L, Huertas-Lopez F, Marti C, Tarazona S, Forteza J, Conesa A, Vicent MJ. Tumor microenvironment-targeted poly-L-glutamic acid-based combination conjugate for enhanced triple negative breast cancer treatment. *Biomaterials* 2018;**186**:8-21.
31. Arroyo-Crespo Juan J, Deladriere C, Nebot Vicent J, Charbonnier D, Masiá E, Paul A, James C, Armiñán A, Vicent María J. Anticancer activity driven by drug linker modification in a Polyglutamic Acid-based combination-drug conjugate. *Adv Funct Mater* 2018;**28**:1800931.
32. Tchou J, Zhao Y, Levine BL, Zhang PJ, Davis MM, Melenhorst JJ, Kulikovskaya I, Brennan AL, Liu X, Lacey SF, Posey AD, Williams AD, et al. Safety and efficacy of intratumoral injections of chimeric antigen receptor (CAR) T cells in metastatic breast cancer. *Cancer Immunol Res* 2017;**5**:1152-61.
33. Tayyari F, Gowda GAN, Olopade OF, Berg R, Yang HH, Lee MP, Ngwa WF, Mittal SK, Raftery D, Mohammed SI. Metabolic profiles of triple-negative and luminal A breast cancer subtypes in African-American identify key metabolic differences. *Oncotarget* 2018;**9**:11677-11690.
34. Beloribi-Djefaflia S, Vasseur S, Guillaumond F. Lipid metabolic reprogramming in cancer cells. *Oncogenesis* 2016;**5**:e189.

35. Manning HC, Buck JR, Cook RS. Mouse Models of Breast Cancer: Platforms for discovering precision imaging diagnostics and future cancer medicine. *J Nucl Med* 2016;**57**:60S-68S.
36. Pereira ER, Kedrin D, Seano G, Gautier O, Meijer EFJ, Jones D, Chin S-M, Kitahara S, Bouta EM, Chang J, Beech E, Jeong H-S, et al. Lymph node metastases can invade local blood vessels, exit the node, and colonize distant organs in mice. *Science* 2018;**359**:1403-1407.
37. Brown M, Assen FP, Leithner A, Abe J, Schachner H, Asfour G, Bago-Horvath Z, Stein JV, Uhrin P, Sixt M, Kerjaschki D. Lymph node blood vessels provide exit routes for metastatic tumor cell dissemination in mice. *Science* 2018;**359**:1408-1411.
38. Zhang XY, Lu WY. Recent advances in lymphatic targeted drug delivery system for tumor metastasis. *Cancer Biol Med* 2014;**11**:247-54.
39. Liu Z, Zhu Y, Wang Y, Fu Q, Fu H, Wang Z, Zhang J, Li G, Xu J, Dai B. Prognostic value of granulocyte colony-stimulating factor in patients with non-metastatic clear cell renal cell carcinoma. *Oncotarget* 2017;**8**:69961-69971.
40. Metcalf D. The colony-stimulating factors and cancer. *Nat Rev Cancer* 2010;**10**:425-34.
41. Lin C-H, Yu J-C, Ou J-J, Lee Y-T, Wu H-S. Leukemoid reaction as a "Tumor Marker" in breast cancer. *Surgical Science* 2012;**3**:271-733.
42. Kowanetz M, Wu X, Lee J, Tan M, Hagenbeek T, Qu X, Yu L, Ross J, Korsisaari N, Cao T, Bou-Reslan H, Kallop D, et al. Granulocyte-colony stimulating factor promotes lung metastasis through mobilization of Ly6G+Ly6C+ granulocytes. *PNAS* 2010;**107**:21248-21255.
43. Jablonska J, Lang S, Sionov RV, Granot Z. The regulation of pre-metastatic niche formation by neutrophils. *Oncotarget* 2017;**8**:112132-112144.
44. Kitamura T, Qian B-Z, Pollard JW. Immune cell promotion of metastasis. *Nat Rev Immunol* 2015;**15**:73-86.
45. Cavanaugh PG, Jia LB, Zou YY, Nicolson GL. Transferrin receptor overexpression enhances transferrin responsiveness and the metastatic growth of a rat mammary adenocarcinoma cell line. *Breast Cancer Res Treat* 1999;**56**:201-15.
46. Nicolson GL, Menter DG, Herrmann J, Cavanaugh P, Jia L, Hamada J-i, Yun Z, Nakajima M, Marchetti D. Tumor metastasis to brain: role of endothelial cells, neurotrophins, and paracrine growth factors. *Crit Rev Oncog* 1994;**5**:451-71.
47. Rodrigues dos Santos C, Fonseca I, Dias S, Mendes de Almeida JC. Plasma level of LDL-cholesterol at diagnosis is a predictor factor of breast tumor progression. *BMC Cancer* 2014;14:132.
48. Wei B, Yao M, Xing C, Wang W, Yao J, Hong Y, Liu Y, Fu P. The neutrophil lymphocyte ratio is associated with breast cancer prognosis: an updated systematic review and meta-analysis. *OncoTargets Ther* 2016;**9**:5567-5575.
49. Johnson CH, Santidrian AF, LeBoeuf SE, Kurczy ME, Rattray NJW, Rattray Z, Warth B, Ritland M, Hoang LT, Loriot C, Higa J, Hansen JE, et al. Metabolomics guided pathway analysis reveals link between cancer metastasis, cholesterol sulfate, and phospholipids. *Cancer Metal* 2017;**5**:9.
50. Galons J-P, Job C, Gillies RJ. Increase of GPC levels in cultured mammalian cells during acidosis. A31P MR spectroscopy study using a continuous bioreactor system. *Magn Reson Med* 1995;**33**:422-4226.

51. Lampa M, Arlt H, He T, Ospina B, Reeves J, Zhang B, Murtie J, Deng G, Barberis C, Hoffmann D, Cheng H, Pollard J, et al. Glutaminase is essential for the growth of triple-negative breast cancer cells with a deregulated glutamine metabolism pathway and its suppression synergizes with mTOR inhibition. *PLoS One* 2017;**12**:e0185092.
52. Tsai IL, Kuo T-C, Ho T-J, Harn Y-C, Wang S-Y, Fu W-M, Kuo C-H, Tseng Y. Metabolomic dynamic analysis of hypoxia in MDA-MB-231 and the comparison with inferred metabolites from transcriptomics data. *Cancers* 2013;**5**:491-510.
53. Puchades-Carrasco L, Jantus-Lewintre E, Pérez-Rambla C, García-García F, Lucas R, Calabuig S, Blasco A, Dopazo J, Camps C, Pineda-Lucena A. Serum metabolomic profiling facilitates the non-invasive identification of metabolic biomarkers associated with the onset and progression of non-small cell lung cancer. *Oncotarget* 2016;**7**:12904-16.
54. Balendiran GK, Dabur R, Fraser D. The role of glutathione in cancer. *Cell Biochem Funct* 2004;**22**:343-352.

Abbreviation List

6-TG:	6-thioguanine
18F-FDG:	18-Fluorodeoxyglucose
ALN:	Axillary Lymph Node(s)
BC:	Breast Cancer
BCAA:	Branched Amino Acids
BLI:	Bioluminescence Imaging
CAA:	Cancer-Associated Adipocytes
DFS:	Disease Free Survival
EH:	Extramedullary Hematopoiesis
ER:	Estrogen Receptor
EPR:	Enhanced Permeability and Retention
FBS:	Fetal Bovine Serum
G-CSF:	Granulocyte-Colony Stimulating Factor
GPC:	Glycerophosphorylcholine
H&E:	Hematoxylin and Eosin
HER2:	Human Epidermal Growth Factor Receptor 2

ILN:	Inguinal Lymph Node
LDL:	Low Density Lipoprotein
MDR:	Multi-Drug Resistance
MPC:	Myeloid Precursor Cell
NOD/SCID:	Non-Obese Diabetic/Severe Combined Immunodeficiency
NLR:	Neutrophil-to-Lymphocyte Ratio
NTA:	Nanoparticle-Tracking Analysis
OPLS-DA:	Orthogonal Projections to Latent Structures Discriminant Analysis
PR:	Progesterone Receptor
PET/CT:	Positron Emission Tomography/Computed Tomography
TAG:	Triacylglycerol
TNBC:	Triple Negative Breast Cancer

FIG-1

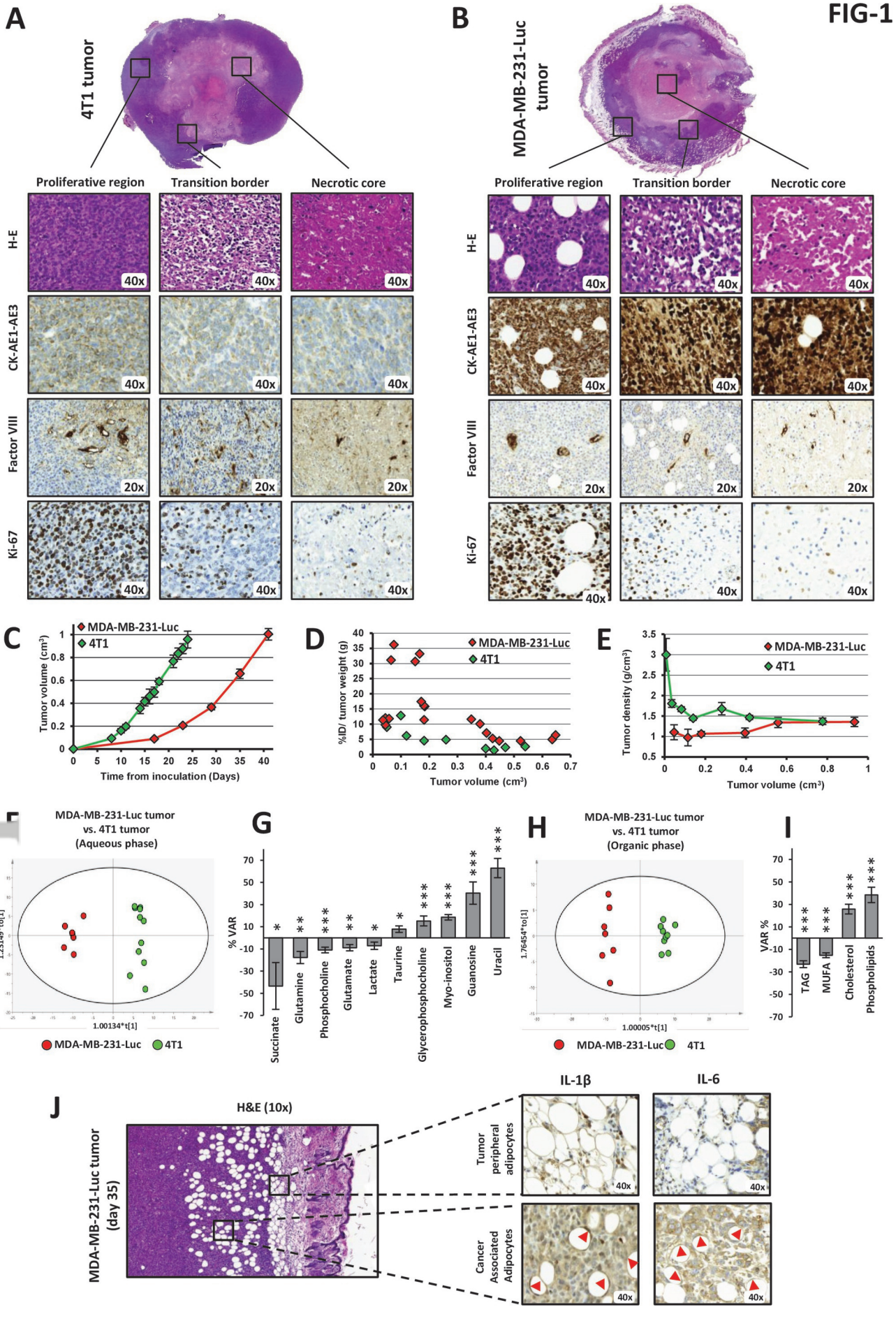

FIG-2

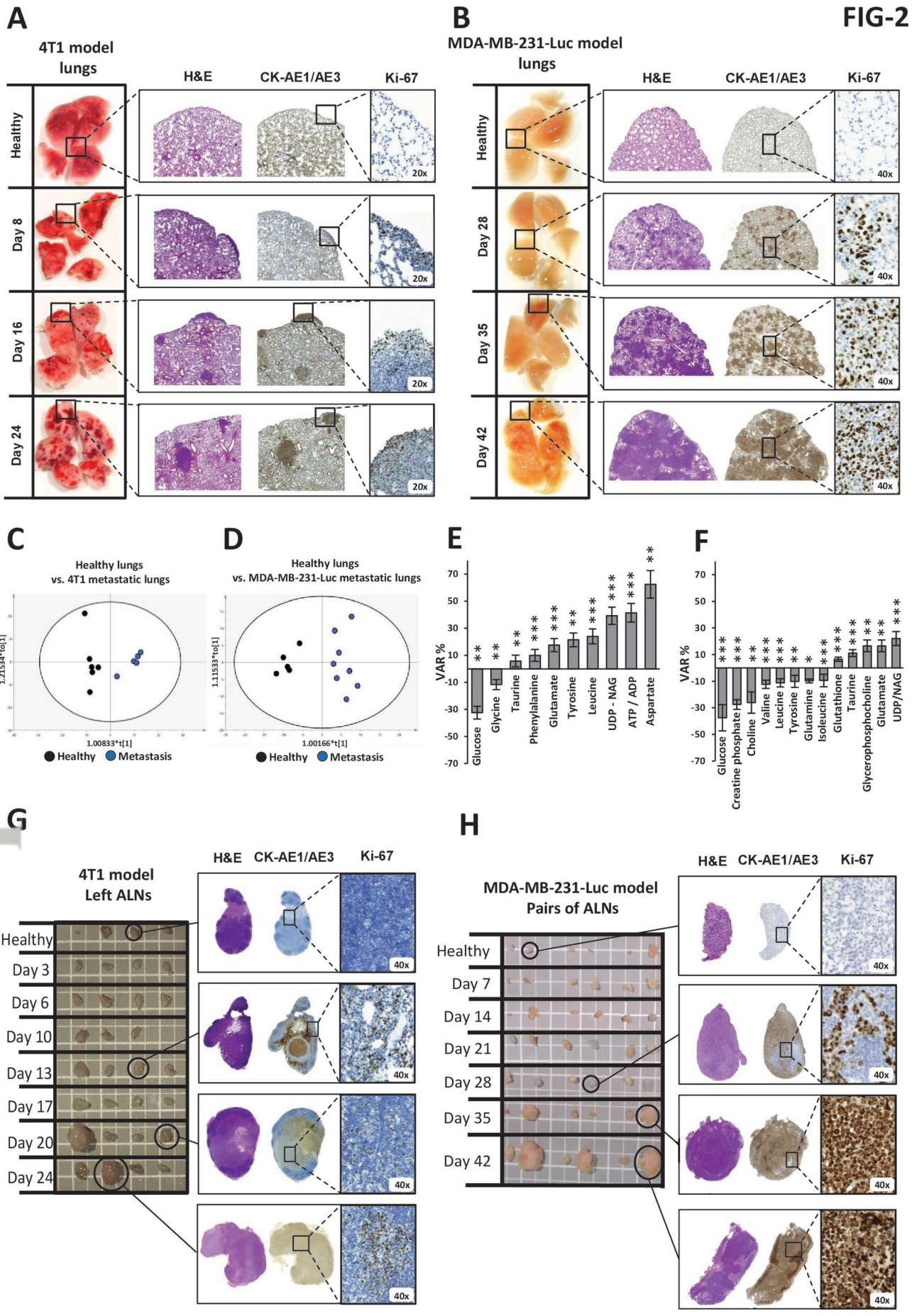

FIG-3

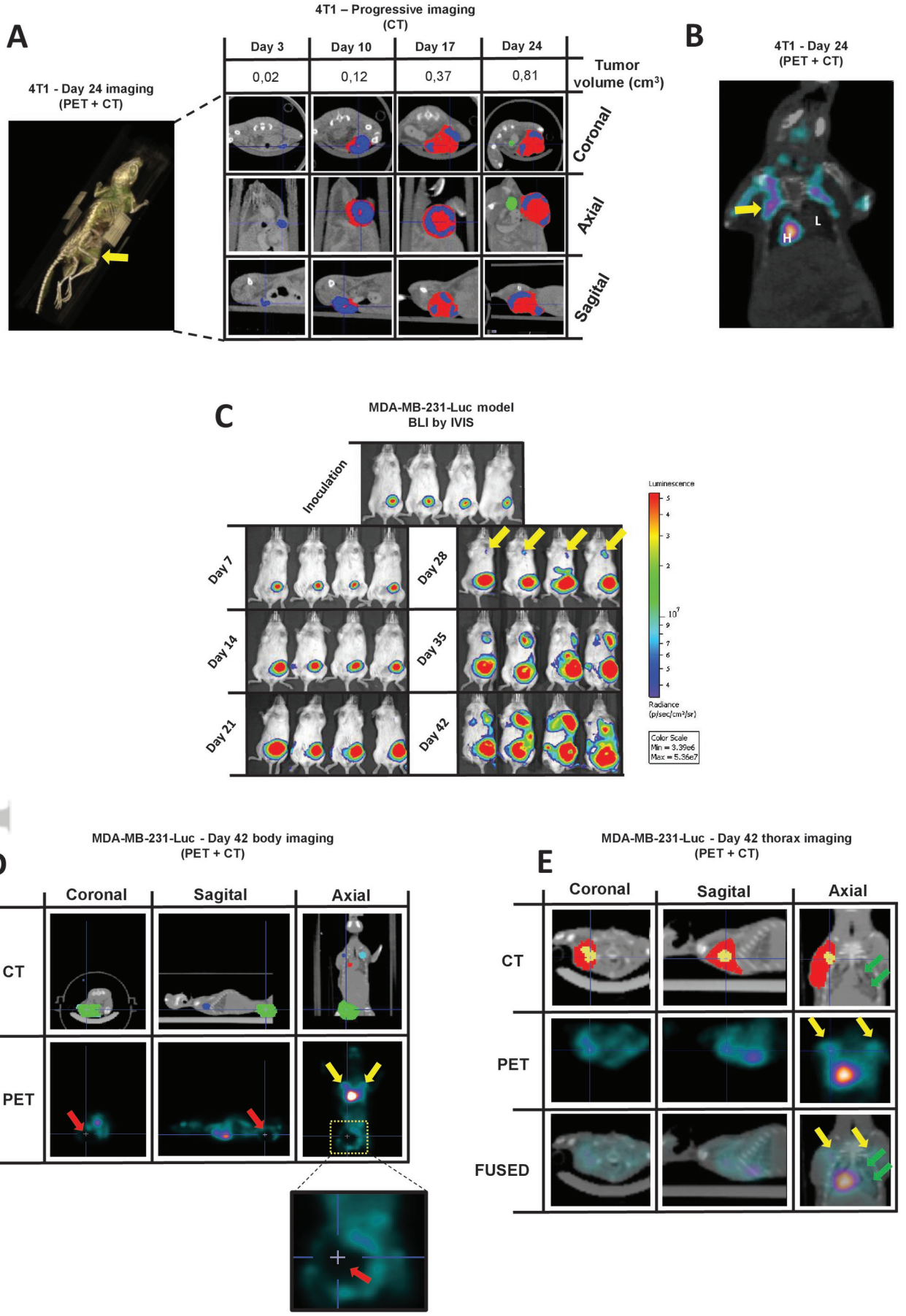

FIG-4

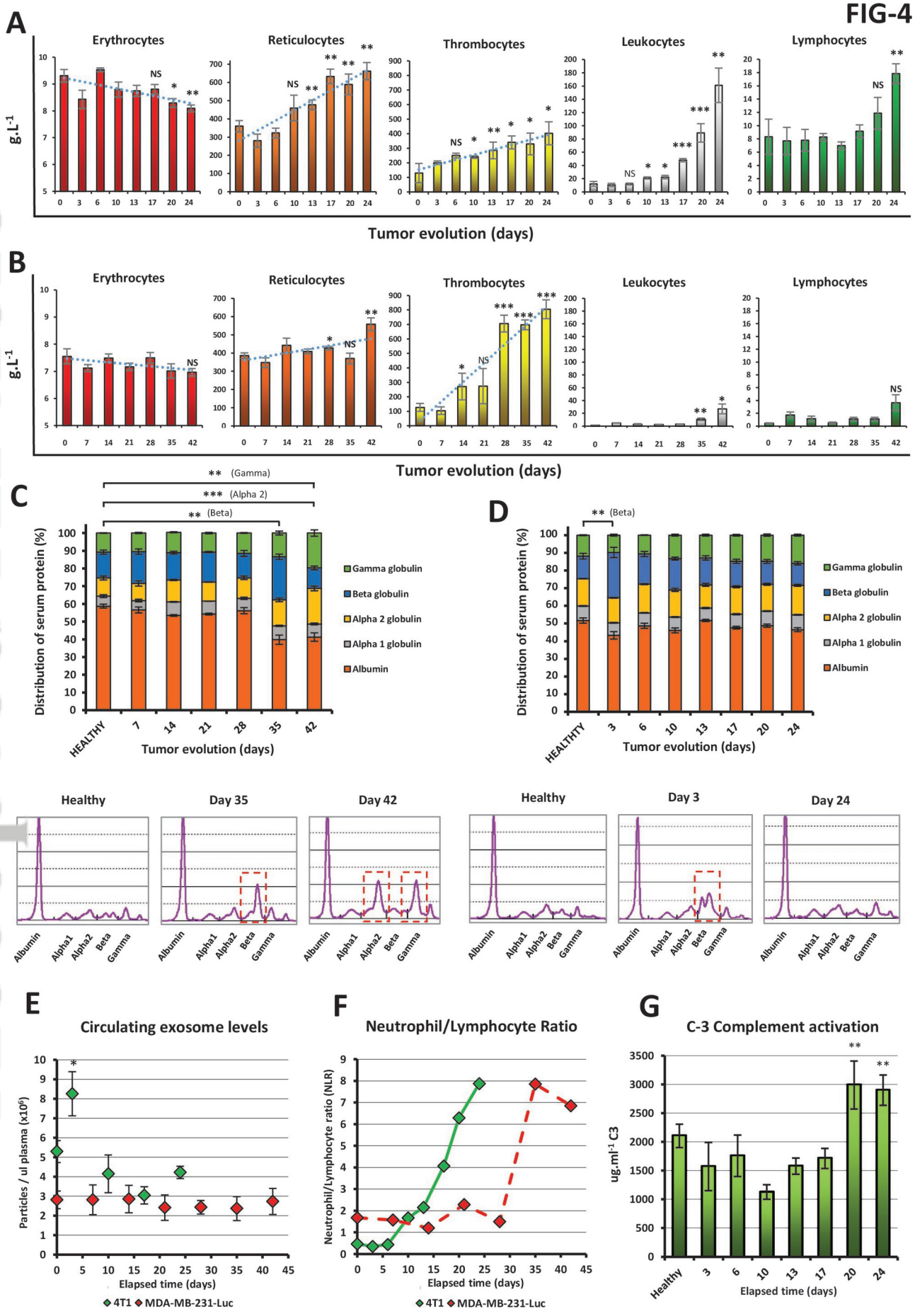

FIG-5

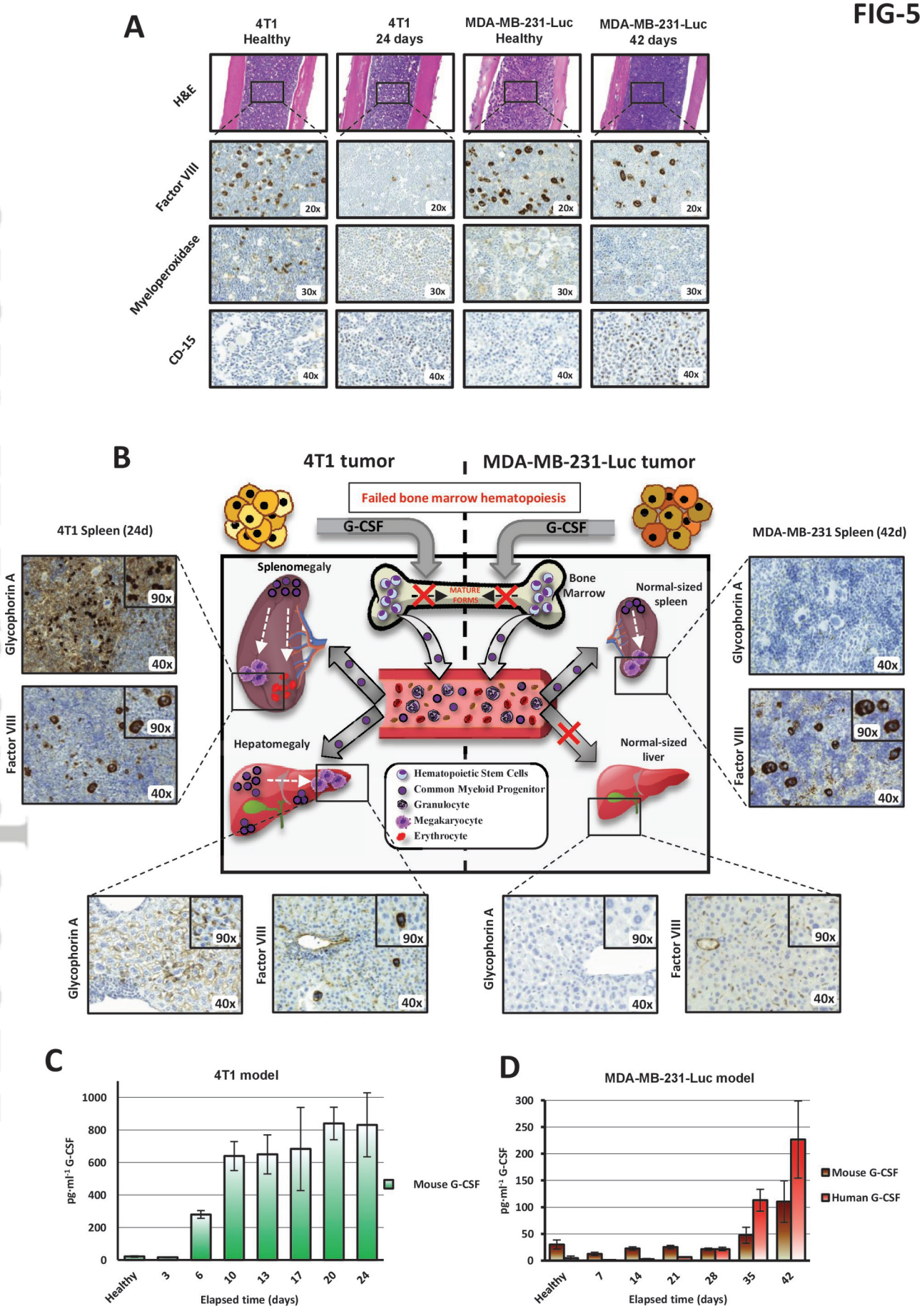

FIG-6

A

TNBC preclinical models: Features and suitability for development of anticancer therapies

BALB/cOlaHsd 4T1 breast carcinoma cell line (murine)	NOD.CB17-Prkdcscid/NCrHsd MDA-MB-231-Luc breast carcinoma (human)
→ Early stage drug discovery (screening)	→ Mid-to-late stage drug discovery (screening)
→ Necrosis and tumor microenvironment studies	→ Studies on relationship between metastasis spread and stromal CAA
→ Faithfully mimicking of stage-specific histological and biochemical aspects of human disease	→ Mimics human disease in immunosuppressed conditions
→ Similar human immune response to tumor	→ Adequate for intratumor administration
→ Suitability for cancer-induced leukocytosis study	→ Metastatic spread by non-invasive imaging techniques (BLI and PET/CT)
→ Preferential lymphatic route for metastatic spread to lung	→ Increased passive accumulation of nanotherapeutics via greater EPR effect
→ Ideal for evaluation of effects on immune surveillance	→ Preferential hematic route for metastatic spread to lung
	→ Facilitates assessment of human biomarkers and predictors

B

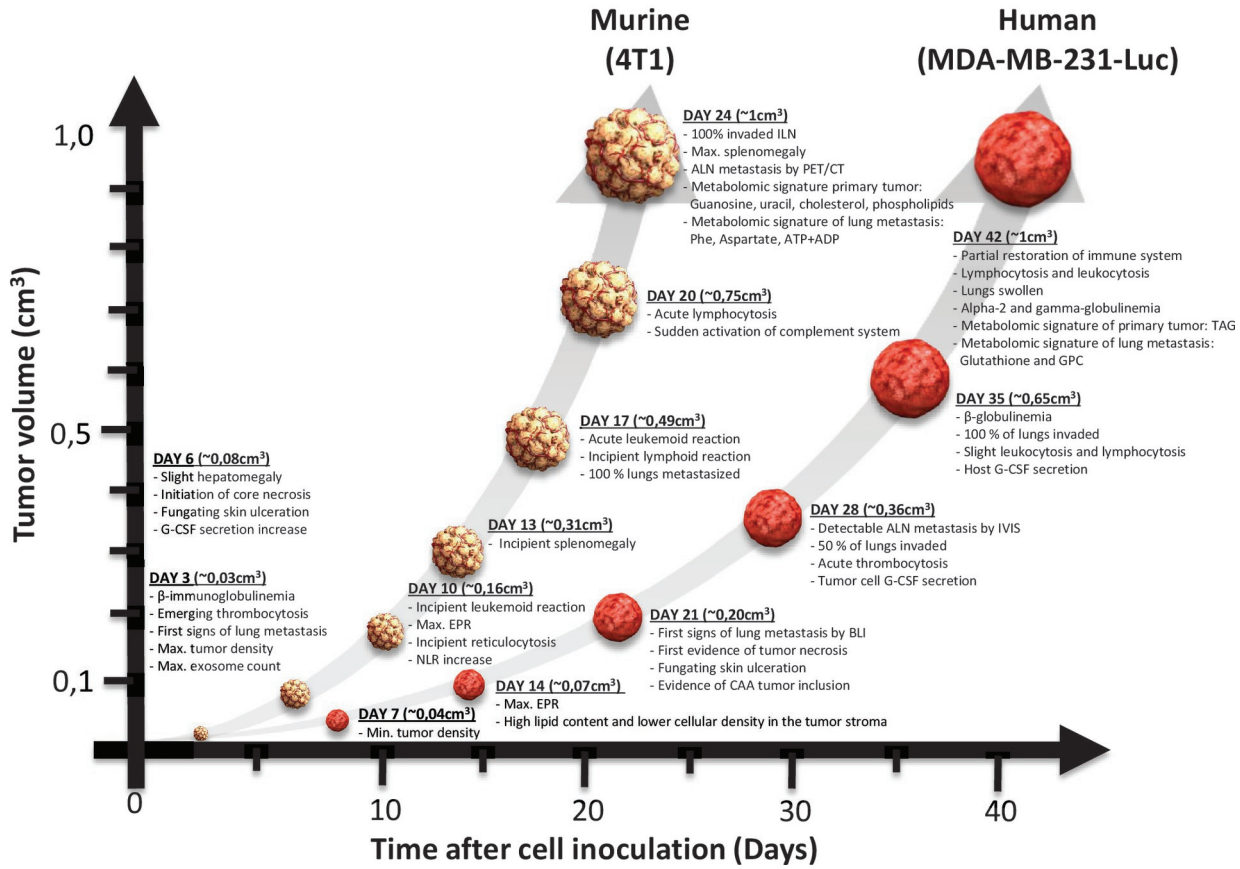

Triple-negative breast cancer (TNBC), an aggressive, metastatic, and recurrent breast cancer subtype, currently lacks adequately described spontaneously metastatic preclinical models that faithfully reproduce the clinical scenario. Here, the authors provide an in-depth comparative analysis of two preclinical spontaneously metastatic TNBC orthotopic models, MDA-MB-231-Luc and 4T1. The results reveal a metastatic switch in both models with immune system activation and serum protein profile reconfiguration, which may support resistance to treatment and recurrence in TNBC. The authors also identify critical functional biomarkers and metabolomic signatures for metastatic progression that may facilitate the development of anti-cancer therapeutics.